Supporting Information

Unleashing potential of novel 2D-Bi_2S_3/1D-SnO_2 heterostructure thin film anode for light-fostered asymmetric electrochromic supercapacitor

Manopriya Samtham[a], Aayushi Miglani[b], Ajay Patil[a], Venkatesh Dharavath[a], Santosh Bimli[a,c], Himanshu Srivastava[d], Ravindra Jangir[d,e], Yuan-Ron Ma[a,f,g], Ram J. Choudhary[h]*, and Rupesh S. Devan,[a,i,j]*

[a] Department of Metallurgical Engineering and Materials Science, Indian Institute of Technology Indore, Simrol, Khandwa Road, 453552, India. rupesh@iiti.ac.in.
[b] Department of Physics, Indian Institute of Technology Indore, Simrol, Khandwa Road, 453552, India.
[c] Department of Chemistry, University of Ulsan, Ulsan, 44610, Republic of Korea.
[d] Accelerator Physics and Synchrotrons Utilization Division, Raja Ramanna Centre for Advanced Technology, Indore, 452013, India.
[e] Homi Bhabha National Institute, BARC Training School Complex, Anushaktinagar, Mumbai, 400094, India.
[f] Department of Applied Informatics, Fo Guang University, Yilan 262307, Taiwan
[g] Department of Physics, National Dong Hwa University, Hualien, 974301, Taiwan.
[h] UGC-DAE Consortium for Scientific Research, Khandwa Road, Indore, 452001, India. ram@csr.res.in.
[i] Center for Electric Vehicles and Intelligent Transport System, Indian Institute of Technology Indore, Simrol, Khandwa Road, 453552, India.
[j] College for Creativity and Technology, Fo Guang University, Yilan 262307, Taiwan

A] Introduction

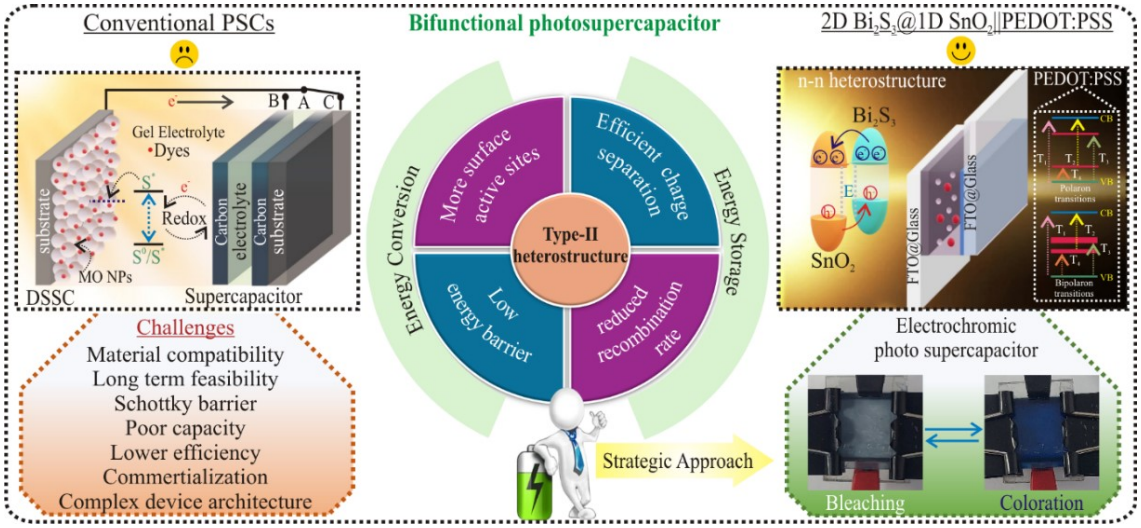

Fig. S1 Schematic illustration of type–II novel 2D Bi_2S_3@1D SnO_2 heterostructure thin film photoanode for light-fostered asymmetric electrochromic supercapacitor.

B] Materials Characterization

The crystal structure and lattice parameters were evaluated from X-ray diffraction (XRD, Empyrean-DY2528, Malvern Panalytical, Cu-K_α λ = 1.54 Å). Raman spectroscopy (HORIBA-JY LABRAM-HR, 532 nm excitation) was employed to investigate the interstitial defect level and crystallinity in pristine SnO_2 and Bi_2S_3@SnO_2 samples. Surface morphology and elemental distribution were analysed using a Field emission scanning electron microscope (FESEM, JEOL, JSM-7610F Plus) and energy-dispersive X-ray spectroscopy (EDS, Oxford, X-MAX). Microstructural and crystallographic features were further investigated using transmission electron microscopy (TEM, Thermo-Fisher, Talos-F200X G2). To investigate the chemical states and electronic structure, the X-ray photoelectron spectroscopy (XPS, monochromated Al K_α, λ = 61 Å) and ultraviolet photoelectron spectroscopy (UPS, AIPES, 450 MeV, I = 100 mA) were conducted using a synchrotron radiation source at Beamline-02, Indus-1, Raja Ramanna Centre for Advanced Technology (RRCAT), Indore. Optical band gaps were estimated using a UV-visible diffused reflectance spectroscopy (DRS, Shimadzu, UV-2600). Electrochemical properties and redox kinetics were evaluated using an electrochemical workstation (Autolab, PGSTAT302N, Metrohm).

C] Experimental details

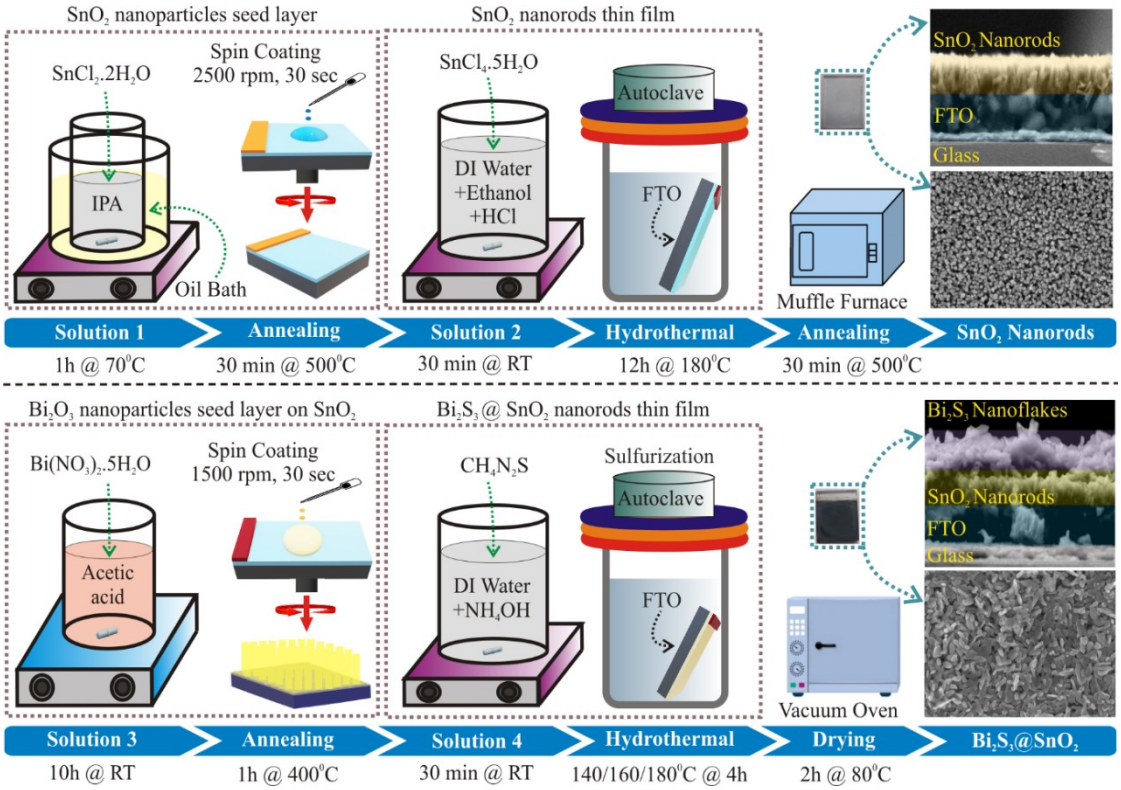

Fig. S2 Schematic representation of the synthesis protocol for 2D Bi_2S_3 NFs@1D SnO_2 NRs heterostructure thin film.

D] Electrochemical measurements

The electrochemical measurements were performed in 1 M Na_2SO_4 aq. electrolyte using standard three-electrode configuration, comprising Bi_2S_3@SnO_2/FTO as the working electrode (WE), Ag/AgCl as the reference electrode (RE), and Pt wire as the CE. Cyclic voltammetry (CV), Galvanostatic Charge Discharge (GCD), and electrochemical impedance spectroscopy (EIS) were employed to evaluate electrochemical behaviour. EIS was recorded at open-circuit potential over a frequency range from 10^5 to 10^{-2} Hz. Photoassisted energy storage performance was assessed using a 300 W Xenon lamp kept in a photo-chem-reactor (100 mW/cm^2) in synchrony with the potentiostat. The areal capacitance (C_A, mF/cm^2) of the electrodes was evaluated from GCD analysis using the formula [1]:

$$C_a = \frac{I \times \Delta t}{A \times \Delta V} \quad (1)$$

Moreover, the performance of the asymmetric device was evaluated in terms of areal capacitance (C_a, mF/cm^2), areal energy density (E_a, Wh/cm^2), and areal power density (P_a, W/cm^2) using equations [2-4]

$$C_a = \frac{2I \times \Delta t}{A \times \Delta V} \quad (2)$$

$$E_a = \frac{1}{2} \times C_A \times \frac{(\Delta V)^2}{3.6} \quad (3)$$

$$P_a = \frac{E_A}{\Delta t} \times 3600 \quad (4)$$

Where I, Δt, A, and ΔV represent the applied current (A), discharge time (s), active area (cm^2), and potential window (V), respectively.

E] Structural analysis using XRD and Raman spectroscopy

The XRD patterns were analysed to investigate the phase composition and crystallographic structure of SNO, BO-SNO, BS14, BS16, BS18, BO-FTO, and B16 thin films, as shown in Fig. S3(a). The bare FTO reveals diffraction peaks at 2θ = 26.3°, 33.5°, 33.6°, 51.3°, 57.8°, 61.4°, and 65.3°, which are attributed to the (110), (101), (200), (211), (202), (310), and (301) planes of FTO substrate (JCPDS No.: 077-0452), which are also consistent with the tetragonal rutile phase of SnO_2 (JCPDS 041-1445). Following the hydrothermal treatment for preparation of SNO, a significant increase in the intensity of (101) and (202) diffraction planes is observed, which represents preferential anisotropic growth of SnO_2 on SnO_2-seeded FTO surface [5]. In the BO-SNO thin film, the additional peaks appear at 27.7°, 32.6°, 46.3°, and 54.3°, which correspond to the (201), (220), (222), and (203) planes of tetragonal β-Bi_2O_3 (JCPDS 027-0050) [6]. Moreover, the low-intense peak at 11.3° corresponds to the (011) plane, which is attributed to minor fraction of the cubic γ-Bi_2O_3 phase (JCPDS 074-1375)[7]. The BS14, BS16, and BS18 thin films, forming Bi_2S_3@SnO_2 bilayer heterostructures, exhibit the additional diffraction peaks at 2θ = 15.6°, 17.3°, 22.2°, 23.5°, 24.9°, 28.4°, 31.7°, 39.7°, and 46.3°, which are assigned to (200), (201), (202), (011), (301), (112), (212), (114), and (314) planes of orthorhombic α–Bi_2S_3 (JCPDS 017-0320) [8], alongside the characteristic peaks of SnO_2 and FTO substrate. The absence of other secondary phases of

Bi_2S_3 confirms the successful formation of Bi_2S_3@SnO_2 bilayer hetero-structure. XRD analysis further verified that the pristine BO-FTO and B16 thin films deposited on FTO substrates in the absence of SnO_2 nanorods preserved their structural phase without any impurities (Fig. S5(a)).

Further, Raman spectra of SNO, BO-SNO, BS14, BS16, and BS18 thin films were recorded in the spectral range of 50 cm^{-1} to 800 cm^{-1} (Fig. S2(b)). Raman bands at 552 cm^{-1} and 633 cm^{-1} in SNO (* marked) are ascribed to non-degenerate A_{1g} mode of the tetragonal rutile SnO_2 phase of FTO substrate [9]. Five distinct Raman modes were observed for BO-SNO, associated with the A_{1g} phonon mode of Bi atoms at 94 cm^{-1}, A_g and B_g modes of minor γ-Bi_2O_3 cubic phase at 125 cm^{-1} and 151 cm^{-1}, respectively [10]. Whereas, 317 cm^{-1}, and 471 cm^{-1} modes are characteristic Bi-O stretching vibrations of β-Bi_2O_3 tetragonal phase, consistent with the XRD results. The Raman spectra of BS14, BS16, and BS18 confirm the formation of orthorhombic α-Bi_2S_3. The modes centered at 55 cm^{-1}, 72 cm^{-1}, 101 cm^{-1}, 186 cm^{-1}, and 237 cm^{-1} are associated with the A_g symmetric modes arising from transverse (in-plane) symmetric stretching vibrations of Bi-S bonds. Similarly, peaks at 83 cm^{-1}, 169 cm^{-1}, and 264 cm^{-1} correspond to the B_{1g} mode of longitudinal (out-of-plane) asymmetric stretching of Bi-S bonds, which are in good agreement with the existing reports [11, 12]. Thus, Raman modes confirm the phase purity and retention of the intrinsic lattice structure of Bi_2S_3 within the Bi_2S_3@SnO_2 bilayer hetero-structure.

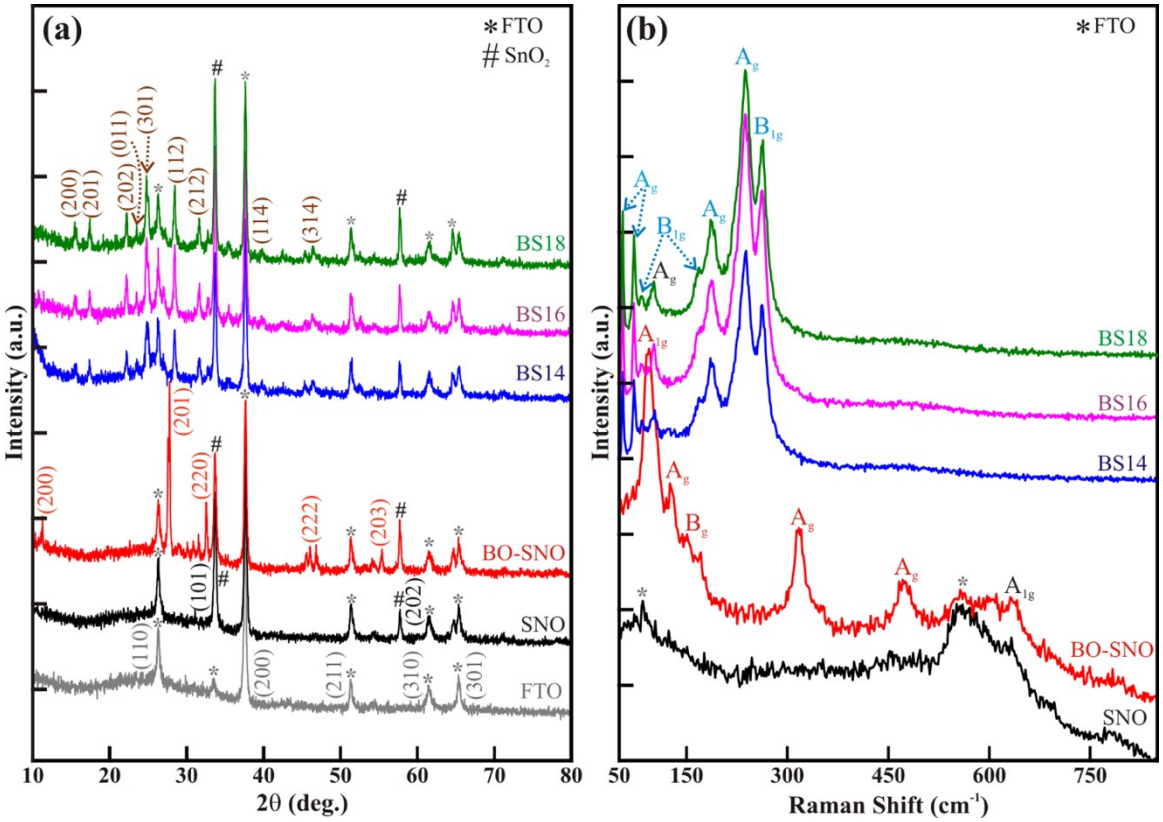

Fig. S3 (a) XRD patterns and (b) Raman spectra of SNO, BO-SNO, BS14, BS16, and BS18.

F] Morphological and elemental analysis.

Fig. S4 illustrates the top-view FE-SEM images of SNO, BO-SNO, BS14, BS16, and BS18 thin films. Uniformly aligned SnO_2 nanorod arrays are vertically grown on FTO substrate, exhibiting an average diameter of 50 nm and length of ~200 nm nm (Fig. S4(a) and

Fig. S5(b)). Notably, after spin coating, granular Bi_2O_3 nanoparticles with average diameter of ~70 nm are densely deposited over the SnO_2 NRs (Fig. S4(b)). Upon hydrothermal sulfurization at 140 °C (BS14), irregular and incomplete growth of Bi_2S_3 nanoparticles is observed, forming an interconnecting network over SnO_2 NRs (Fig. S4(c,d)). Increasing sulfurization temperature to 160 °C (BS16) resulted in the evolution of a relatively dense, yet irregular, 2D Bi_2S_3 nano-structure network (Fig. S4(e,f) and Fig. S5(c)). Further increase in temperature to 180 °C (BS18) resulted in the growth of randomly oriented petals-like nanoflakes with >100 nm length, which uniformly covered the SNO NRs (Fig. S4(g,h)). Thiourea, serving as a sulphur source, also acts as structure directing agent by providing high density of nucleation sites that facilitate the transformation from NPs to nanoflakes within the Bi_2S_3@SnO_2 bilayer heterostructure. Importantly, a micronized island network of Bi_2O_3, formed dense and rough film on bare FTO (Fig. S5(d)), which further transformed into densely packed 2D Bi_2S_3 flakes at 160 °C (Fig. S5(e)). This observation confirms the engrossment of SNO NRs in directing the transformation from nanoparticle network to well-defined petal-like 2D Bi_2S_3 flakes, forming the Bi_2S_3/SnO_2 hetero-structure. Further, EDS spectra and elemental mapping of all samples confirm the presence and spatial distribution of Sn, O, Bi, and S elements (Fig. S5(f,g)). Overall, 2D Bi_2S_3 nanostructures decorated on 1D SnO_2 NRs provide ample accessible electroactive sites, ensuring shorter ion diffusion pathways in the electrolyte. This architecture facilitates enhanced redox kinetics and effective charge carrier transport, which significantly promotes light harvesting and contributes to improving photo-assisted electrochemical performance.

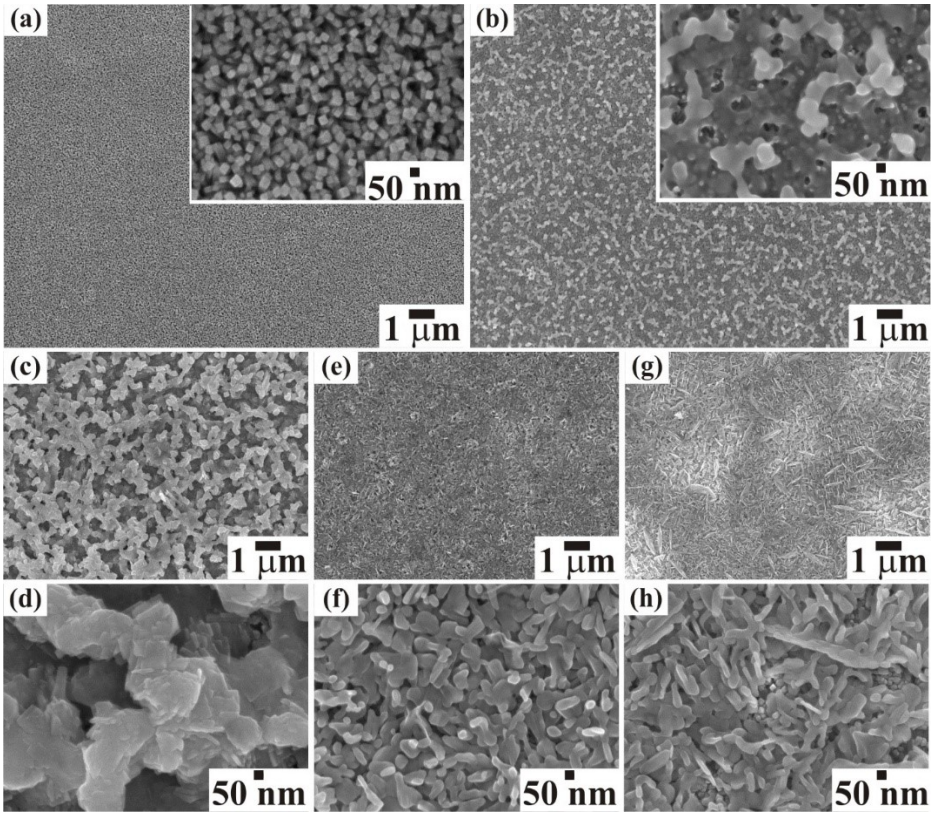

Fig. S4 FE-SEM images of (a) SNO, (b) BO-SNO, (c, d) BS14, (e, f) BS16, and (g, h) BS18 grown over the FTO-coated glass substrates.

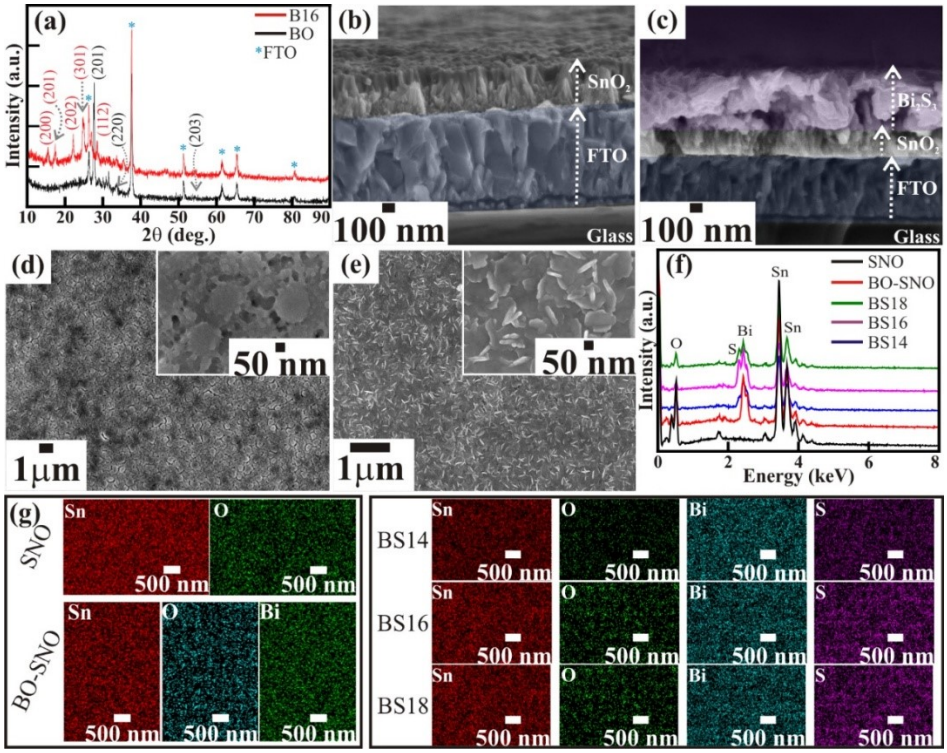

Fig. S5 (a) XRD patterns of BO and B16 films coated on FTO. Cross-section FE-SEM images of (b) SnO_2, (c) BS16. FE-SEM images of (d) bare BO and (e) B16. (f) EDS spectra of SNO, BO-SNO, BS14, BS16, and BS18 samples, and (g) corresponding mapping images for Sn, O, Bi, and S elements.

G] Growth mechanism of 2D Bi_2S_3@1D SnO_2 bilayer heterostructure

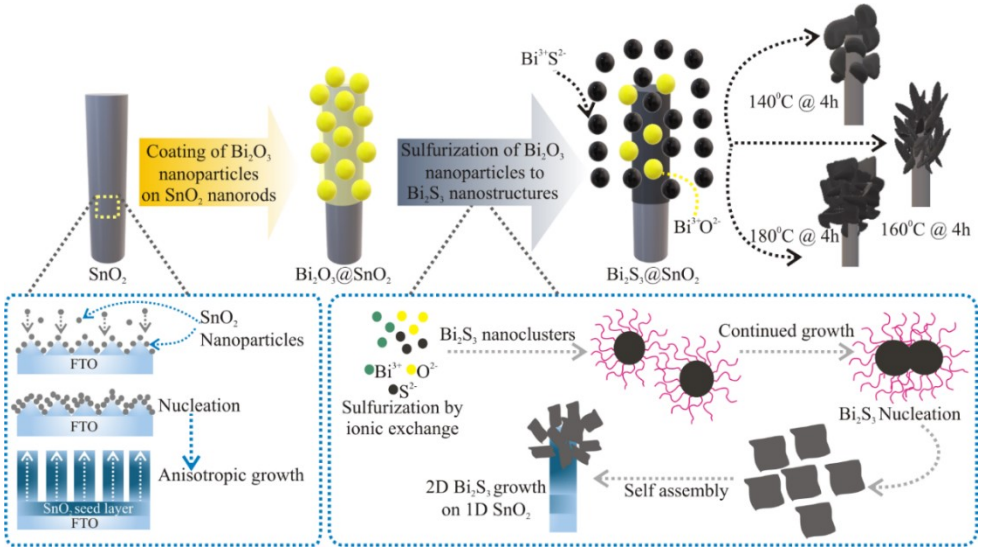

Fig. S6 Schematic growth mechanism of pristine SnO_2 NRs and 2D Bi_2S_3 NFs@1D SnO_2 NRs heterostructure thin film by hydrothermal process.

The hydrothermal synthesis of SnO_2 NRs involves hydrolysis, condensation, nucleation, and anisotropic crystal growth, governed by acidic aqueous environment. Upon dissolution in DI water and ethanol mixture, $SnCl_4$ undergoes controlled hydrolysis, forming tin hydroxide species [13]:

$SnCl_4 + 4H_2O \rightarrow Sn(OH)_4 + 4HCl$ (5)

$Sn(OH)_4 \rightarrow SnO_2 + 2H_2O$ (6)

Ethanol modulates the hydrolysis rate, while protonation in dilute HCl forms $[Sn\text{-}OH_2]^+$ species that condense into SnO_2 nuclei [13, 14]. Preferential adsorption of Cl^- ions promotes anisotropic growth of SnO_2 nanorods along the (101) direction during high-temperature crystallization. Subsequently, the 2D Bi_2S_3 nanostructure grows on the SnO_2 NRs via hydrothermal sulfurization using thiourea as sulfur source in aqueous ammonia. Thiourea undergoes hydrolysis and dissociation as follows [2, 15]:

$CH_4N_2S + NH_4OH + H_2O \rightarrow 3NH_3 + CO_2 + H_2S \uparrow$ (7)

$H_2S \rightarrow 2H^+ + S^{2-}$ (8)

$Bi_2O_3 \rightarrow 2Bi^{3+} + 3O^{2-}$ (9)

$2Bi^{3+} + 3S^{2-} \rightarrow Bi_2S_3 + H_2O$ (10)

At an elevated temperature, thiourea undergoes hydrolysis and protonation to form H_2S, which subsequently dissociates into sulfide ions (S^{2-}) [16]. Concurrently, Bi^{3+} cations dissociated from Bi_2O_3 react with S^{2-} during hydrothermal vulcanization, facilitating Bi_2S_3 nucleation via ionic exchange assisted reduction mechanism [16]. The resulting Bi_2S_3 nuclei aggregate into nanoparticles to minimize surface free energy following the Gibbs principle. These Bi_2S_3 nanoparticles further evolve into 2D Bi_2S_3 nanostructures through oriented attachment and self-assembly, which are thermodynamically favourable under given synthesis conditions. To probe this transformation, hydrothermal reactions were carried out at 140, 160, and 180 °C to elucidate the temperature-dependent morphological evolution of Bi_2S_3.

H] Elemental analysis using XPS

The charge states of the elements present in the SNO, BO-SNO, and BS16 thin films were probed through XPS spectra. The spectra were deconvoluted using a Voigt fitting function with a Shirley background. The Sn(3d) spectrum (Fig. S7(a)) exhibits two prominent peaks at binding energy (B.E.) of 486.9 eV(≡ a) and 494.8 eV (≡ b), corresponding to spin orbit split states $3d_{5/2}$ and $3d_{3/2}$, respectively. The binding energy positions of $3d_{5/2}$ and $3d_{3/2}$ and spin-orbital separation of 8.4 eV between these peaks divulge the Sn^{4+} oxidation state, as expected for SnO_2 phase [17]. The O(1s) core level spectrum for SNO (Fig. S7(b)) represents two distinct peaks located at 530.4 eV(≡ c) and 532.2 eV(≡ d), attributed to crystal lattice oxygen (O^{2-}) and surface adsorbed hydroxyl group, respectively [18], confirming the formation of phase-pure SnO_2. Similarly, the Bi(4f) spectrum of BO-SNO (Fig. S7(c)) is deconvoluted into four peaks positioned at 156.7 eV(≡ g), 158.6 eV(≡ e), 162.2 eV(≡ h), and 163.9 eV(≡ f), corresponding to $Bi^0(4f_{7/2})$, $Bi^{3+}(4f_{7/2})$, $Bi^0(4f_{5/2})$, and $Bi^{3+}(4f_{5/2})$, respectively. The presence of relatively very low intensity of $Bi^0(4f_{7/2})$ and $Bi^0(4f_{5/2})$ peaks signifies a small amount of unreacted metallic Bi^0, consistent with literature reports [19]. The corresponding O(1s) spectrum (Fig. S7(d)) shows two distinct peaks at 529.6 eV(≡ c_1) and 531.1 eV(≡ d_1), assigned to lattice oxygen (O^{2-}) and surface hydroxyl group, respectively. Upon sulfurization of BO, S(2p) peaks corresponding to $S^{2-}(4p_{5/2})$ and $S^{2-}(2p_{3/2})$ appear at 160.7 eV(≡ s′) and 161.8 eV(≡ s′′), respectively (Fig. S7(e)) [20]. Additionally, highly intense peaks at 158.2 eV(≡ e_2) and 163.5 eV(≡ f_2) confirm that the Bi^{3+} states remain unchanged after oxygen replacement with sulfur. The B.E. values positioned at 159.4 eV (≡ g_2) and 164.9 eV(≡ h_2) are attributed to $Bi^{5+}(4f_{7/2})$ and $Bi^{5+}(4f_{5/2})$, respectively,

which signifies the existence of very small amount of approximately 7% of Bi^{+5} ions. The O (1s) spectrum after sulfurization (Fig. S7(f)) shifted to higher B.E. at 531.1 eV (≡ c_2), corresponding to sulfate ions (SO_4^{2-}), along with an associated surface hydroxyl group (532.8 eV ≡ d_2). Overall, the XPS analysis confirms the conversion of Bi_2O_3 into Bi_2S_3 upon sulfurization.

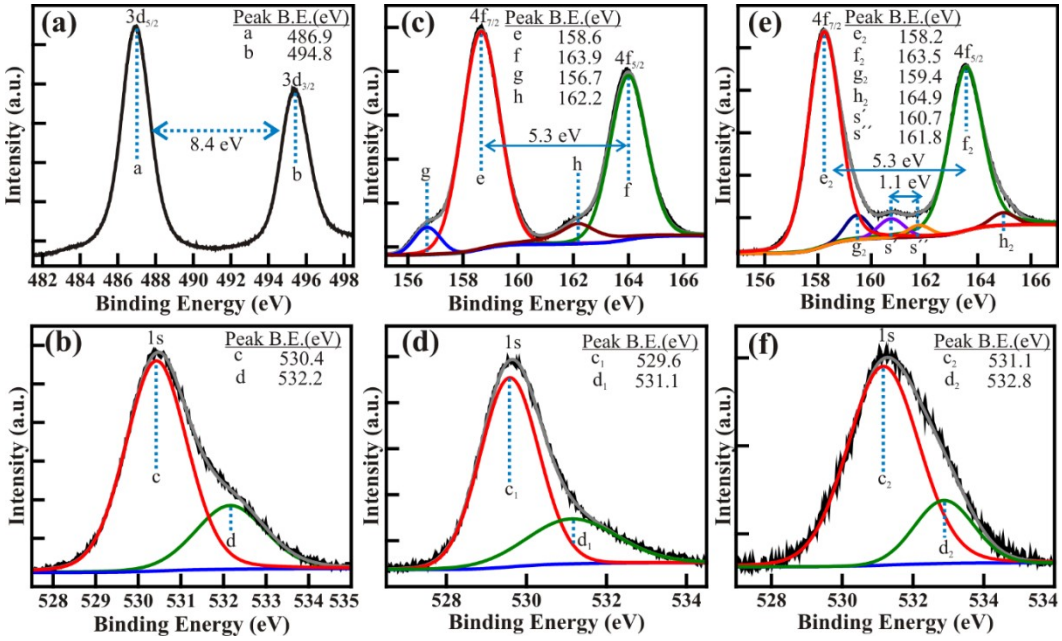

Fig. S7 XPS spectra of (a) Sn(3d) and (b) O(1s) core levels of SNO. (c) Bi(4f) and (d) O(1s) core levels of BO-SNO. (e) Bi(4f) with S (2p) and (f) O(1s) core levels of BS16 thin films.

I] Electrochemical analysis in 3-electrode configuration in 1M Na_2SO_4 electrolyte

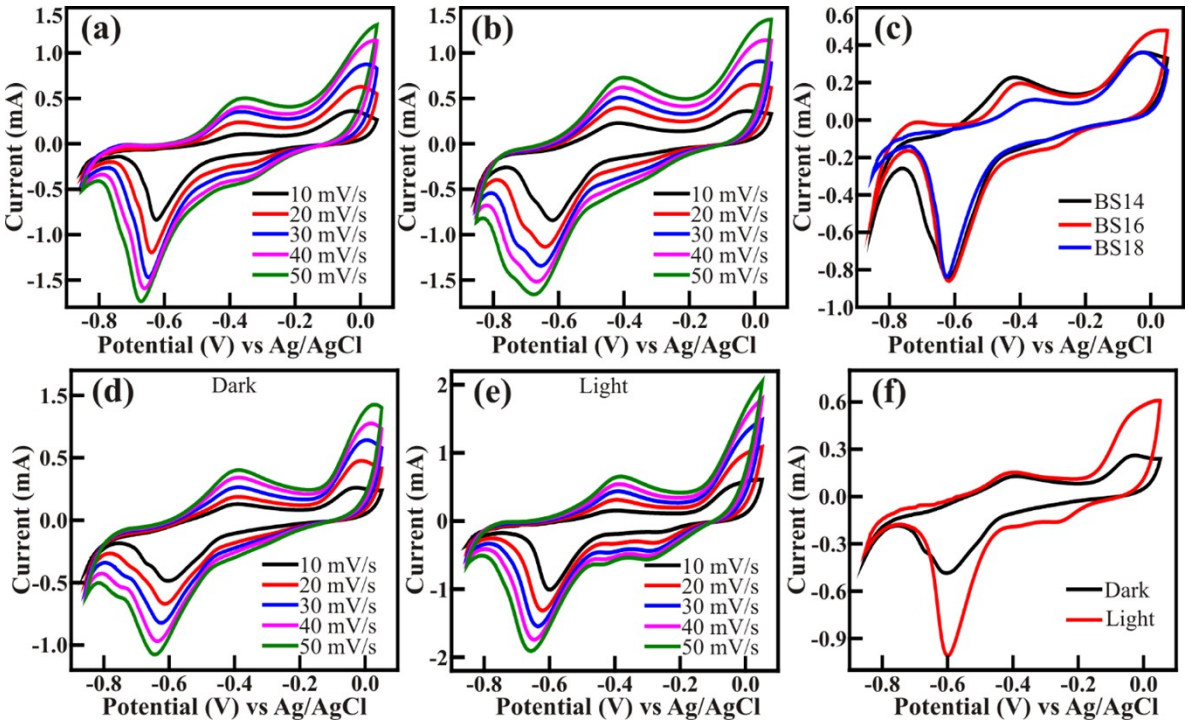

Fig. S8 CV profiles of (a) BS14 and (b) BS18 recorded at various scan rates from 10–50 mVs^{-1}. (c) CV profiles of BS14, BS16, and BS18 recorded at 10 mV/s. (d) CV profiles of BS16 recorded under (d) dark, (e) illumination conditions, and (f) comparison at 10 mV/s.

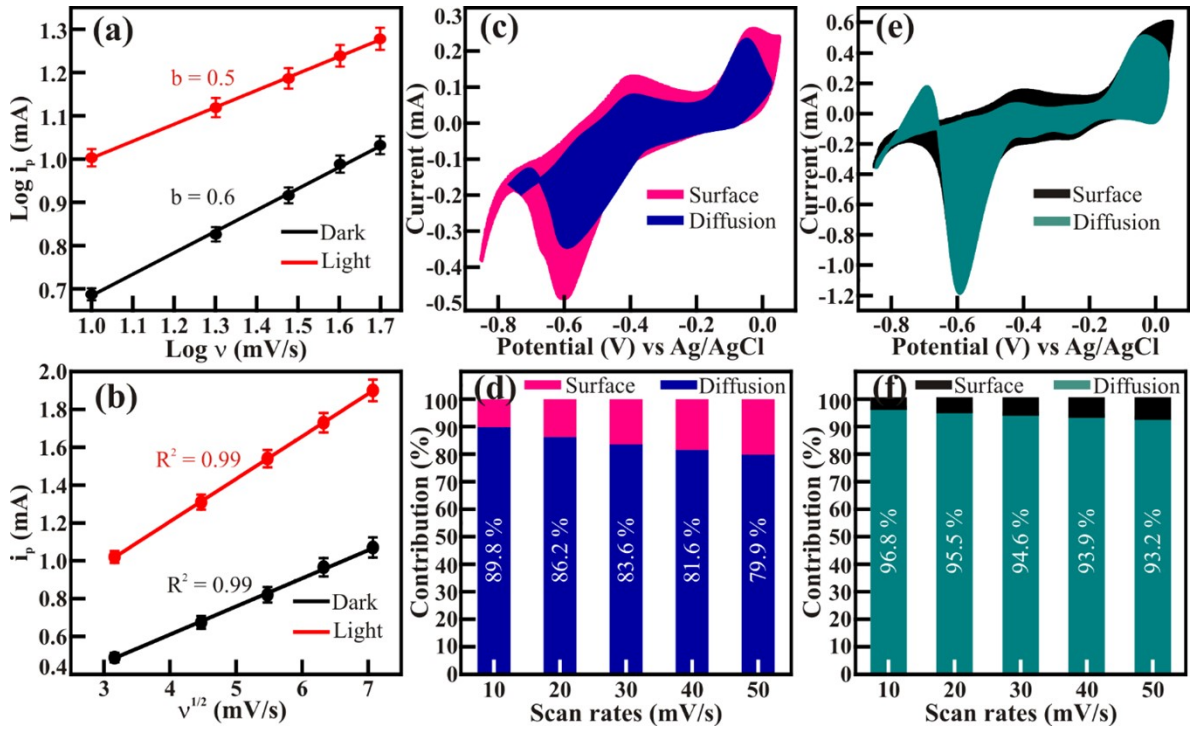

Fig. S9 Anodic peak current density (i_p) variation with respect to (a) scan rate (ν) and (b) square root of scan rate ($ν^{1/2}$) under dark and light. Capacitive and diffusion contribution of BS16 electrodes at 10 mV/s under (c) dark and (d) illumination. Capacitive and diffusion-controlled contributions of BS16 electrode in CV profiles at different scan rates under(e) dark and (f) illumination.

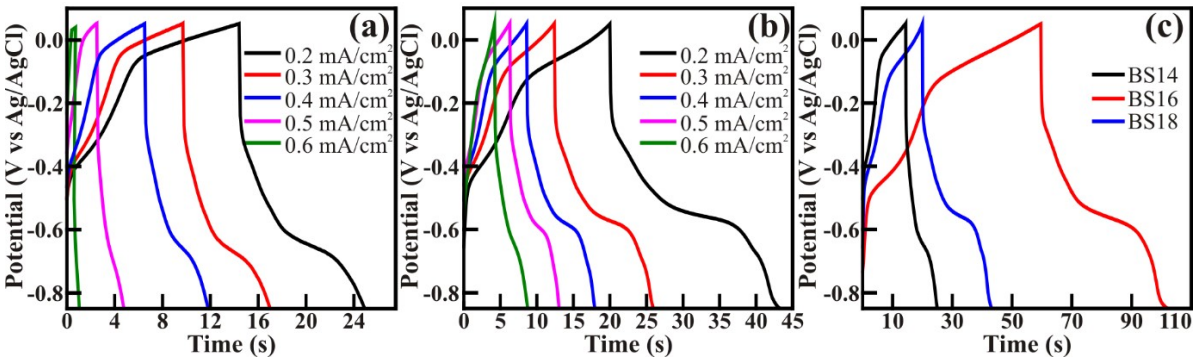

Fig. S10 (a) GCD of (d) BS14 and (b) BS18 recorded at various current densities (0.2–0.6 mA/cm^2). (c) GCD of BS14, BS16, and BS18 recorded at 0.2 mA/cm^2.

Table 2. Parameters acquired from the fitted EIS equivalent circuit for the BS16 heterostructure electrode in the three-electrode configuration.

Parameters	Dark (Stability)		Light (Stability)	
	Before	After	Before	After
R_S (Ω)	23.97	24.26	18.12	27.32
CPE_{dl} ($F.s^{(n-1)} \times 10^{-3}$)	0.29	0.44	0.41	0.54
n	0.89	1	0.88	0.96
R_{ct} (kΩ)	1.72	7.95	4.91	9.42
Z_w (Ω)	64.9	109.7	47.3	106

J] Post-electrochemical analysis

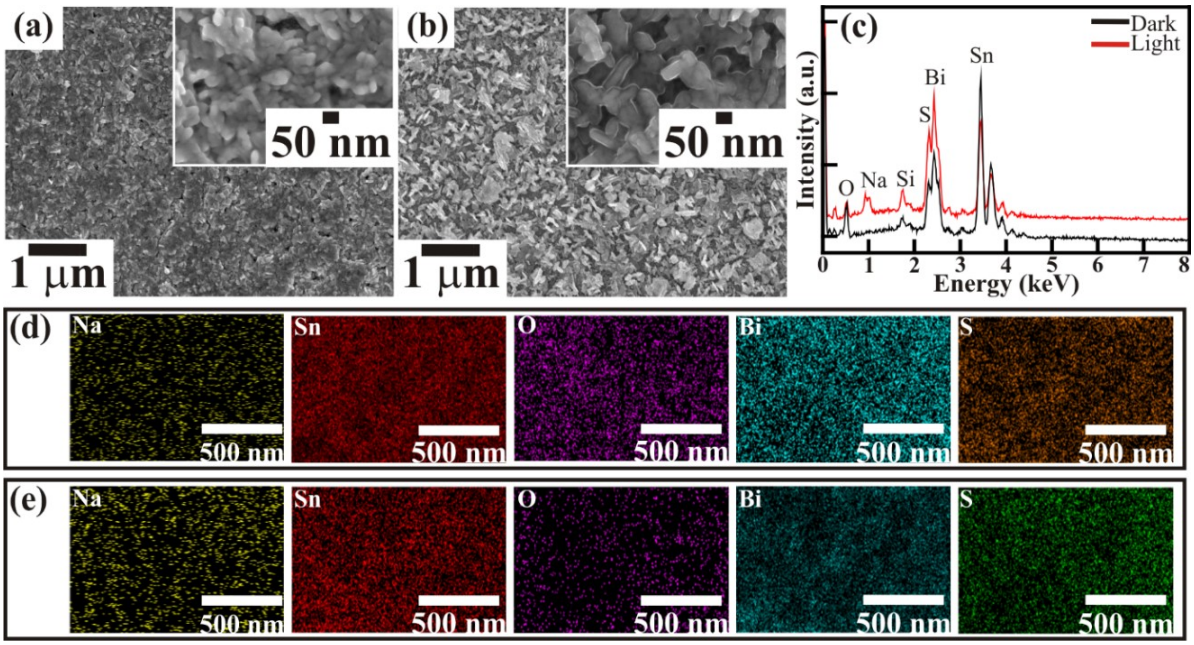

Fig. S11 FE-SEM image of BS16 electrode after stability studies for 2000 cycles under (a) dark and (b) light. Corresponding post-stability (c) EDS spectra and elemental mapping images (d) under dark and (e) illumination.

K] Electrochemical analysis of asymmetric electrochromic supercapacitor device (APSD)

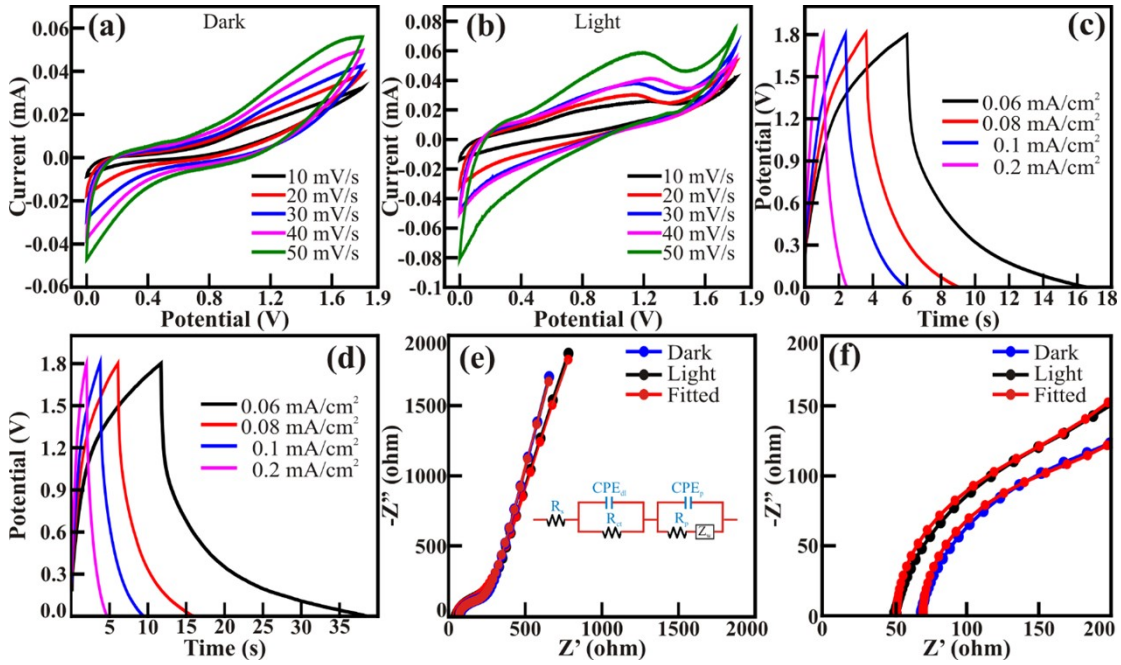

Fig. S12 (a, b) Scan rate dependent CV curves, (c, d) current density dependent GCD curves, and (e, f) Nyquist plots of the asymmetric electrochromic supercapacitor device under dark and illumination.

L] Post-electrochemical analysis

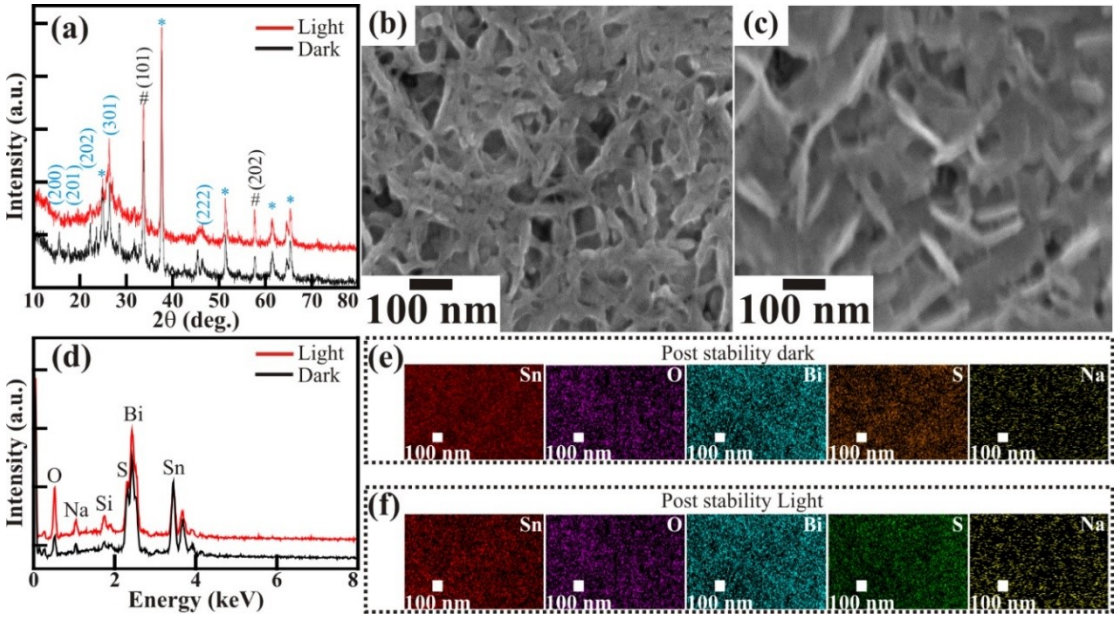

Fig. S13 Post stability (a) XRD patterns, FE-SEM images under (b) dark and (c) illumination, (d) EDS spectra, and elemental mapping images under (e) dark and (f) illumination for the BS16 electrodes of the asymmetric electrochromic supercapacitor device.

Table 3. Comparative electrochemical performances under illumination of photo-rechargeable supercapacitors fabricated on FTO substrate reported in the literature.

Electrode	Electrolyte	C_S	E_d and P_d	Stability	Ref
$MA_3Bi_2I_9$||$MA_3Bi_2I_9$	CPH-G gel	0.28 mF/cm^2 @ 0.01 mA/cm^2	0.04μWh/cm^2, 5.6 mW/cm^2	94.79% @5000	[21]
V_2O_5/ZnO||V_2O_5/ZnO	PVA/KCl	15 μF/cm^2 @ 0.2 μA/cm^2	1.8 nWh/cm^2, 80 nW/cm^2	78% @5000	[22]
ZnO/Ag_2S/ZnS/PEDOT|| PEDOT	PVP/[HEMIm][BF_4]	0.33 mF/cm^2 @ 4 μA/cm^2	-	-	[23]
ZnO||ZnO	PVA/LiCl	40 mF/g @ 1.1 mA/g	78 mWh/kg, 4 mW/kg	80% @3000	[24]
ZnO/CdS||ZnO/CdS	$BMIMBF_4$	22.1 μF/cm^2 @ 2 1 μA/cm^2	2.85 nWh/cm^2, 0.4 μW/cm^2	90% @5000	[25]
Fe_2O_3/$Ni(OH)_2$/PW||CC	1M KCl	2.16 mF/cm^2 @ 0.13 mA/cm^2	-	-	[26]
V_2O_5||V_2O_5	0.5 M K_2SO_4	122 mC/cm^2 @ 0.1 mA/cm^2	9.8 Wh/kg, 29 W/kg		[27]
MoCo@$BiVO_4$||MoCo@ $BiVO_4$	PVA/KCl	16.3 mF/cm^2@ 0.04 mA/cm^2	-	-	[28]
Bi_2S_3@SnO_2||PEDOT:PSS	1M Na_2SO_4	1.78 mF/cm^2 @ 0.06 mA/cm^2	0.8 mWh/cm^2, 356 mW/cm^2	77.2% @1000	**This Work**

M] Electrochemical analysis of pristine PEDOT:PSS electrode in 3-electrode configuration in 1M Na_2SO_4 electrolyte

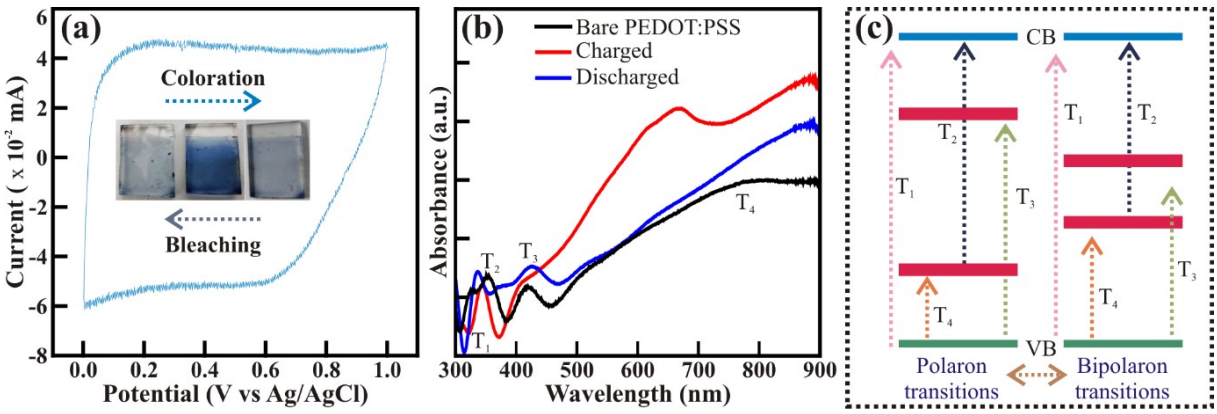

Fig. S14 (a) CV profile BS16||PEDOT:PSS at 50 mV/s in 1M Na_2SO_4 using 3-electrode configuration, and (b) UV-Visible spectra and (c) corresponding electronic transitions of PEDOT:PSS electrode.

References

1. M. Samtham, D. Singh, K. Hareesh and R. S. Devan, *J. Energy Storage*, 2022, **51**, 104418.
2. D. Singh, M. Samtham, N. Bisht, E. Choudhary, V. Kumar, R. Jangir, N. Sonnathi, S. S. Hosmani, A. Katre and R. S. Devan, *Electrochim. Acta*, 2024, **506**, 144998.
3. N. Kitchamsetti, M. Samtham, P. N. Didwal, D. Kumar, D. Singh, S. Bimli, P. R. Chikate, D. A. Basha, S. Kumar, C.-J. Park, S. Chakraborty and R. S. Devan, *J. Power Sources*, 2022, **538**, 231525.
4. N. Kitchamsetti, M. Samtham, D. Singh, E. Choudhary, S. R. Rondiya, Y.-R. Ma, R. W. Cross, N. Y. Dzade and R. S. Devan, *J. Electroanal. Chem*, 2023, **936**, 117359.
5. X. Zhang, Y. Rui, Y. Wang, J. Xu, H. Wang, Q. Zhang and P. Müller-Buschbaum, *J. Power Sources*, 2018, **402**, 460-467.
6. H.-Y. Jiang, P. Li, G. liu, J. Ye and J. Lin, *J. Mater. Chem. A*, 2015, **3**, 5119-5125.
7. G. Liu, S. Li, Y. Lu, J. Zhang, Z. Feng and C. Li, *J. Alloys. Compd*, 2016, **689**, 787-799.
8. H. M. Danamah, T. M. Al-Hejri, V. V. Jadhav, Z. A. Shaikh, T. A. J. Siddiqui, S. F. Shaikh and R. S. Mane, *Dalton. Trans.*, 2024, **53**, 10318-10327.
9. A. Diéguez, A. Romano-Rodríguez, A. Vilà and J. R. Morante, *J. App. Phys*, 2001, **90**, 1550-1557.
10. C. Díaz-Guerra, P. Almodóvar, M. Camacho-López, S. Camacho-López and J. Piqueras, *J. Alloys. Compd*, 2017, **723**, 520-526.
11. U. Chalapathi, B. P. Reddy, T. V. M. Sreekanth and S.-H. Park, *Int. J. Hydrog. Energy*, 2022, **47**, 32796-32803.
12. Y. Guo, Q. Zhao, Z. Yao, K. Si, Y. Zhou and X. Xu, *Nanotechnology*, 2017, **28**, 335602.
13. T. Gupta, Samriti, J. Cho and J. Prakash, *Mater. Today Chem*, 2021, **20**, 100428.
14. M. H. Nguyen and K.-S. Kim, *J. Ind. Eng. Chem.*, 2021, **104**, 445-457.
15. H. M. Danamah, V. V. Jadhav, T. M. Al-Hejri, S. F. Shaikh, A. M. Al-Enizi and R. S. Mane, *J. Energy Storage*, 2024, **97**, 112323.
16. H. M. Danamah, Z. A. Shaikh, T. M. Al-Hejri, T. A. J. Siddiqui, V. V. Jadhav and R. S. Mane, *J. Energy Storage*, 2024, **78**, 109820.
17. S. Bimli, S. R. Mulani, E. Choudhary, V. Manjunath, P. Shinde, S. R. Jadkar and R. S. Devan, *Int. J. Hydrog. Energy*, 2024, **51**, 1497-1507.

18. A. Patil, M. Samtham, E. Choudhary, A. Yadav, A. Miglani, S. Bimli, H. Jadhav and R. S. Devan, *Int. J. Hydrog. Energy*, 2025, **112**, 408-417.
19. X. Zhou, X. Zhang, L. Mo, X. Zhou and Q. Wu, *Small*, 2020, **16**, 1907333.
20. N. S. Kumar, J. S. Kumar, E. Choudhary, S. Bimli, M. Samtham, V. Manjunath, H. Jadhav and R. S. Devan, *Chin. J. Phys*, 2025, **94**, 226-240.
21. I. K. Popoola, M. A. Gondal, A. Popoola and L. E. Oloore, *J. Energy Storage*, 2022, **53**, 105167.
22. P. S. Chauhan, S. Kumar, A. Mondal, P. Sharma, M. N. Parekh, V. Panwar, A. M. Rao and A. Misra, *J. Materials Chemistry A*, 2023, **11**, 95-107.
23. D. Solís-Cortés, E. Navarrete-Astorga, R. Schrebler, J. J. Peinado-Pérez, F. Martín, J. R. Ramos-Barrado and E. A. Dalchiele, *RSC Adv*, 2020, **10**, 5712-5721.
24. C. T. Altaf, O. Coskun, A. Kumtepe, A. M. Rostas, I. Iatsunskyi, E. Coy, E. Erdem, M. Sankir and N. D. Sankir, *Sci. Rep.*, 2022, **12**, 11487.
25. A. D. Mahapatra, S. Kumar, A. Sutradhar, S. Sahoo and A. Misra, *Electrochim. Acta*, 2024, **474**, 143507.
26. M. Mohammadian, S. Rashid-Nadimi and Z. Peimanifard, *Journal of Power Sources*, 2019, **426**, 40-46.
27. H. C. Prakash, M. S. Kumar, T.-W. Lin and S. K. Batabyal, *Electrochimica Acta*, 2023, **469**, 143229.
28. A. S. Renani, Z. Hosseini, D. Eberhart, A. W. Maijenburg and M. M. Momeni, *J. Power Sources*, 2025, **640**, 236687.